Assessing Charge Carrier Trapping in Silicon Nanowires Using Picosecond Conductivity Measurements

Ronald Ulbricht

FOM Institute AMOLF, Amsterdam, Science Park 104, 1098 XG Amsterdam, Netherlands

Rufi Kurstjens

IMEC vzw, Kapeldreef 75, 3001 Leuven, Belgium, and Department of Electrical Engineering (ESAT/INSYS), K.U. Leuven, Kasteelpark Arenberg 10, 3001 Leuven, Belgium

Mischa Bonn*

FOM Institute AMOLF, Amsterdam, Science Park 104, 1098 XG Amsterdam, Netherlands, and Max Planck Institute for Polymer Research, Ackermannweg 10, 55128 Mainz, Germany

ABSTRACT: Free-standing semiconductor nanowires on bulk substrates are increasingly being explored as building blocks for novel optoelectronic devices such as tandem solar cells. Although carrier transport properties, such as mobility and trap densities, are essential for such applications, it has remained challenging to quantify these properties. Here, we report on a method that permits the direct, contact-free quantification of nanowire carrier diffusivity and trap densities in thin (~25 nm wide) silicon nanowires—without any additional processing steps such as transfer of wires onto a substrate. The approach relies on the very different terahertz (THz) conductivity response of photoinjected carriers within the silicon nanowires from those in the silicon substrate. This allows quantifying both the picosecond dynamics and the efficiency of charge carrier transport from the silicon nanowires into the silicon substrate. Varying the excitation density allows for quantification of nanowire trap densities: for sufficiently low excitation fluences the diffusion process stalls because the majority of charge carriers become trapped at nanowire surface defects. Using a model that includes these effects, we determine both the diffusion constant and the nanowire trap density. The trap density is found to be orders of magnitude larger than the charge carrier density that would be generated by AM1.5 sunlight.

KEYWORDS: Silicon nanowires, solar cell, defect, surface passivation, terahertz spectroscopy
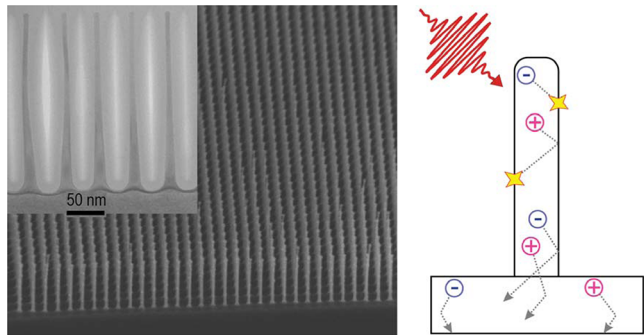
Over the past years silicon nanowires (NWs) have been explored extensively as components of solar cells in an effort to evaluate their potential for next generation, high efficiency, and low cost photovoltaics.[1] Potential advantages of Si NWs for solar cells include light trapping effects to increase light absorption[2,3] and the possibility to engineer radial p−n junctions, allowing to decouple the direction of light absorption from the direction of charge collection.[4−6] These advantages offered by the NW architecture reduce the requirements on the quality and the quantity of the Si that are needed. Another attractive aspect of the NW device architecture is that the underlying material properties are still those of bulk Si, with its high intrinsic conductivity. Hence, many efforts are geared toward cheaper single junction c-Si solar cells based on NWs. The properties of NWs with respect to charge carrier transport are yet to be fully explored, though their high surface/volume ratio raises questions about the influence of surface states. The potential use of these NWs as absorber material for a solar cell depends critically on the quality of the Si NW interface, given the inherent extended interface region. The interface quality will determine the lifetime and mobility of minority carriers and hence the collection efficiency of photogenerated carriers. Furthermore, different ways exist of passivating surface states, and quantifying the remaining defect density is still challenging. For the silicon NWs investigated here, electron spin resonance (ESR) measurements have revealed the presence of a substantial inherent density of Pb_0 ($Si_3{\equiv}Si$) defects (dangling bonds) at the NW Si/SiO_2 interfaces, most likely due to faceting and enhanced interface strain from the oxidation.[7] To quantify the effect of these inherent defects on the lifetime and

mobility of charge carriers generated in the NWs, we employ time-resolved terahertz spectroscopy to probe the behavior of photogenerated carriers on picosecond time scales.

Exciting the NWs at oblique incidence of 45° using a femtosecond laser pulse with photon energies of 4.6 eV, we generate charge carriers across the direct bandgap. The short absorption lengths at this wavelength allow for predominant excitation of the NWs, with only a small fraction of the excitation light reaching the substrate where it generates additional charge carriers. The resulting charge density gradient between NWs and substrate drives diffusion of carriers from the NWs into the substrate. As shown below, the charge carrier conductivity in the bulk substrate is many times larger than that in the wires, due to spatial confinement of carriers in the wires. Thus, the time-dependent conductivity, measured on picosecond time scales using terahertz (THz) probe pulses, allows us to follow the transport of photoexcited carriers from the wires to the bulk phase. More importantly, the number of carriers reaching the bulk phase allows us to quantify the losses associated with this transport as a result of carrier trapping at the surface of the NWs. We model this process using a simple simulation of charge diffusion and trapping, which considers the initial photoexcited charge density gradient, transport from the wire to the bulk substrate, and carrier trapping into NW surface defects. The data in conjunction with the model provide the carrier diffusion coefficient and the density of NW traps. Surprisingly, the trap density is found to be around 10^9 cm^{-2}, 2 orders of magnitude lower than the surface defect density as measured by ESR, depending only slightly on the type of oxide layer on the NW surface. Despite the apparently low density of active traps, the trap density is prohibitively high for photovoltaic applications of the thin NWs presented here.

Experimental Section. Several methods exist to fabricate Si nanowires. We employ a combination of deep UV lithography and dry etching. The target dimension after dry etching is set around 40 nm, and further size reduction is achieved by thermal oxidation. The material used is (100)-oriented 1−10 Ω·cm p-type Cz Si wafers of 300 mm diameter. No intentional doping is introduced before dry etching. First the patterning stack is deposited on the wafer. The pillars are defined by double-patterning a mask consisting of 45 nm lines with a 90 nm pitch by deep UV lithography. The mask is rotated ∼91° between the two exposures in order to obtain a staggered array of dots in the resist. Subsequent dry etching with different etch chemistries is performed to transfer the pattern through each of the layers of the patterning stack. The final Si etch is performed with a mixture of SF$_6$, CH$_2$F$_2$, and N$_2$/He. After the Si etch a dry in-situ strip is performed to remove residual hard mask.

The Si NW core diameter is further reduced by rapid thermal oxidation at 1150 °C for 60 s in an O$_2$/N$_2$ ambient in two steps. After a first oxidation, the oxide is removed in a dry NF$_3$/NH$_3$-based chemical etch. The second oxidation step is a repetition of the first. The final size of the diameter of the NWs can be tuned by a combination of dry etching and thermal oxidation. The NWs used in this study had a tapered profile of 500 nm high, 36 nm diameter at the bottom and 12 nm diameter at the top (see Figure 1). For the SEM imaging the thermal oxide was removed by vapor HF to be able to measure the size of the c-Si cores.

The NWs become flexible once the thickness becomes less than 20 nm, as is apparent in Figure 1, where in addition effects from the electron beam and charging may play a role. To keep
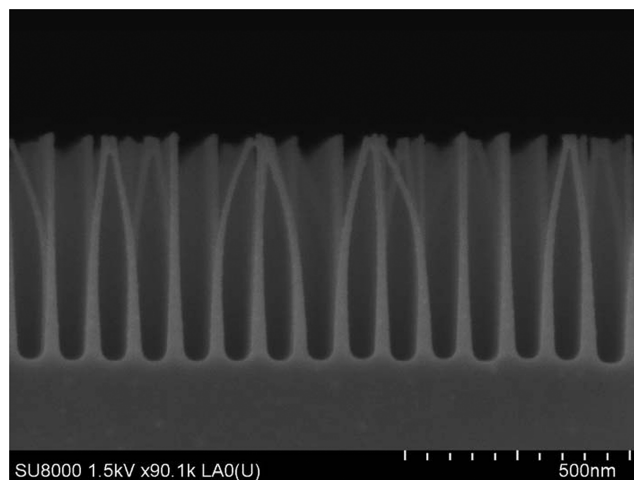

Figure 1. Scanning electron microscope image of the nanowires after thermal oxidation. The thermal oxide was removed by vapor HF for this SEM image, which causes the NWs to bend; for the terahertz spectroscopy the oxide was present.

the NWs aligned and prevent bending and breaking, the thermal oxide is left on the NWs for the terahertz measurements. Additionally, the interwire space was filled with a-SiO$_2$ using a cycled plasma enhanced chemical vapor deposition at 200 °C.

After oxidation two different samples were prepared: On the first sample (sample 1), depassivation of dangling bonds was achieved by annealing in nitrogen at 700 °C for 30 min. On the second sample (sample 2) dangling bond passivation was performed by applying a forming gas anneal (95% N$_2$, 5% H$_2$ gas) at 400 °C for 30 min.

The time-resolved THz setup is pumped by an amplified Ti:sapphire laser system that delivers 800 nm (1.55 eV), 100 fs pulses at 3 W of output power and a repetition rate of 1 kHz. Light pulses at 266 nm (4.6 eV), generated by frequency-tripling the fundamental using two 1 mm thick BBO crystals, is used to photoinject carriers into the silicon NWs. The polarization of the 266 nm beam could be rotated using a half-wave plate. Single-cycle THz pulses are subsequently used to measure the frequency-dependent conductivity with subpico-second time resolution. The generation and detection of the THz probe are accomplished by nonlinear optical rectification and electro-optic detection, respectively, using femtosecond 800 nm pulses in two 1 mm thick ZnTe crystals.[8] The complex THz photoconductivity spectra were measured by recording the transmitted THz electric field $E(t)$ through the unexcited sample and the photomodulated differential THz field $\Delta E(t)$ and employing a frequency domain analysis of these transients.[8] The charge density dynamics were measured by probing the excitation-modulated differential signal at the peak of the THz field. In this way, predominantly the real part of the photoconductivity, i.e., the photoinduced change in absorption, which is proportional to the charge density, is measured at a frequency of ∼0.6 THz. We verified that the influence of the phase shift of the THz waveform (caused by the imaginary part of the photoconductivity) on this differential signal is negligible. This is also readily calculated from the comparable sizes of the real and imaginary contributions to the complex conductivity (Figure 3a).

Results and Discussion. Figure 2 shows the time evolution of the real part of the photoconductivity at 0.6 THz after
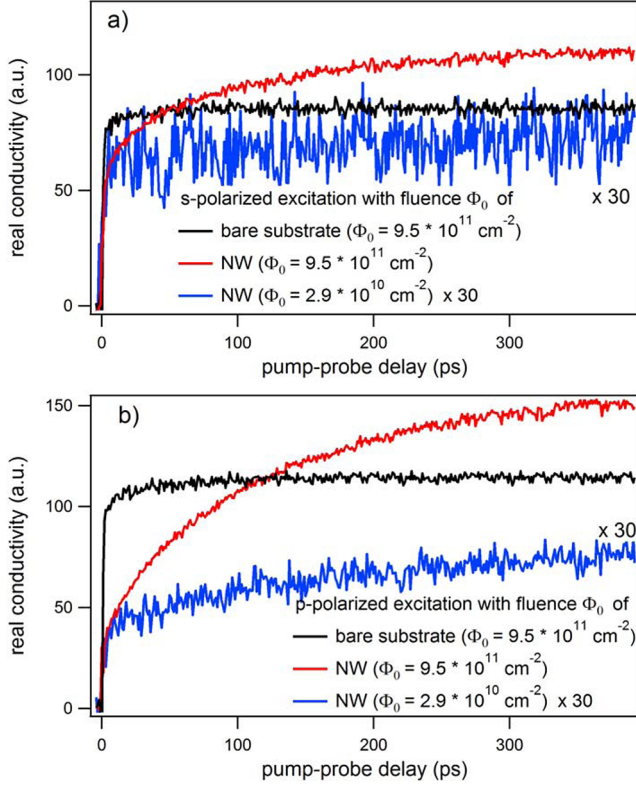
Figure 2. Dynamics of the THz real conductivity of silicon NWs on bulk silicon after excitation with 266 nm light at an angle of 45° for (a) s-polarized excitation light and (b) p-polarized excitation and a photon flux Φ_0 of 9.5×10^{11} cm^{-2} (black and red traces). Black traces show excitation of the bare substrate, whereas red and yellow traces show NW excitation. The yellow traces is the real photoconductivity for NW excitation at a reduced photon flux of 2.9×10^{10} cm^{-2}, rescaled by factor 30.

exciting sample 1 with photon energies of 4.6 eV (266 nm) and fluences Φ_0 of 9.5×10^{11} photons·cm^{-2} (black and red traces) and Φ_0 of 2.9×10^{10} photons·cm^{-2} (yellow trace) at an angle of 45°. Figure 2a shows the results for s-polarized excitation light (field perpendicular to wires) and Figure 2b for p-polarization (excitation E-field parallel to wires). The black trace shows the measured photoconductivity when exciting the sample on the backside, also at 45° incidence, i.e., directly injecting carriers into the silicon substrate. As expected for an indirect semiconductor, for which recombination is slow, the conductivity increases quasi-instantaneously at pump−probe delay $\tau_p = 0$, to remain constant within the 400 ps time window. We note that there is a small (∼10%) additional increase of the photoconductivity on ∼10 ps time scales, which we attribute to carrier cooling and intervalley scattering of carriers into lower-lying conduction bands that presumably results in a change of the carrier scattering time and/or effective mass, thereby increasing the measured photoconductivity. The signal is larger for p-polarized light since the reflection is smaller, and thus more light is absorbed in the substrate. When the NW layer is excited with the same fluence (red traces), the initial signals are smaller due to the much reduced THz conductivity of carriers in the NWs (see model below). The conductivity shows an instantaneous component, attributed to light directly reaching the substrate, and a slow rise of the photoconductivity on ∼100 ps time scales, attributed to carriers reaching the bulk phase from the NWs. Interestingly, s-polarized light generates a larger

initial response than p-polarized light, conversely to the substrate excitation, while the degree of increase is more pronounced for p-polarized light. The final photoconductivity after 400 ps is larger for both pump polarizations as compared to the substrate excitation. The blue traces in both graphs show the rescaled real conductivity for a fluence of 2.9×10^{10} cm^{-2}, i.e., about 30 times lower than the fluence from the red trace. Here, the initial step (attributed to direct substrate excitation) scales with the fluence, but a greatly reduced increase is visible for p-polarized excitation and no increase is present for s-polarization, pointing to the predominance of direct bulk excitation. This change in the dynamics can be understood by noting that trapping of charge carriers occurs in the NWs, which, in particular at low excitation densities, prevents carriers generated in the wires to reach the bulk. At higher excitation densities the traps get saturated, and carriers can reach the bulk phase on ∼100 ps time scales.

In order to gain more insight into these intricate dynamics, it is useful to look at the frequency-resolved complex photoconductivities provided by the broadband THz probe spectrum. The frequency dependence of the conductivity for charge carriers in bulk and NWs is expected to be different and the discrimination of both thus possible.[8]

The bulk penetration depth for 266 nm light is around 5 nm and the length of the NW layer along the optical pathway is 700 nm for 45° excitation. Hence, since the excitation layer is smaller than 1 μm, i.e., many orders of magnitude smaller than the THz wavelength, we can use the thin-film approximation to extract the complex conductivity $\hat{\sigma}_{\text{tot}}(\omega)$ at various pump−probe delays τ_p.[9]

The overall conductivity will be composed of contributions from charge carriers in the NWs $\hat{\sigma}_{\text{nw}}(\omega)$ and those in the underlying bulk substrate $\hat{\sigma}_{\text{bulk}}(\omega)$:

$$\hat{\sigma}_{\text{tot}}(\omega) = \hat{\sigma}_{\text{bulk}}(\omega) + \hat{\sigma}_{\text{nw}}(\omega)$$

For charge carriers in the bare substrate the conductivity $\hat{\sigma}_{\text{bulk}}(\omega)$ can be described well using the Drude model:[10]

$$\hat{\sigma}_{\text{bulk}}(\omega) = \frac{N_s e^2 / \varepsilon_0 m^*}{1 - i\omega\tau_s}$$

Here, N_s is the charge carrier density, ε_0 the free space permittivity, e the electric charge, m^* the carrier effective mass ($= 0.27 m_0$ for the electron), and τ_s the carrier scattering time. The extracted scattering time is somewhat reduced for higher charge densities due to increased likelihood of electron−hole scattering events.[11] From experiments where the substrate is directly excited, we find values between 150 fs for the highest excitation densities and 210 fs for the lowest ones used in the experiments.

Charge carriers in NWs respond differently to the THz probe than in bulk. In such a confined geometry carriers experience a restoring force which results in a shift of the conductivity response (centered at zero for the Drude response) to higher frequencies. Depending on the exact conditions and the consequential physical origin of this restoring force, one can describe this situation by either plasmon resonances,[12−14] embedding the Drude model in an effective medium[15] or applying a generalized version such as the Drude−Smith model.[16] For all these models a Lorentzian oscillator provides a good approximation of the NW charge response in the THz probe window:

$$\hat{\sigma}_{\mathrm{nw}}(\omega) = \frac{a}{1 - i\tau_{\mathrm{nw}}\omega(1 - \omega_{\mathrm{r}}^2/\omega^2)}$$

Here, a denotes the magnitude of the NW contribution, τ_{nw} the carrier scattering time in the NWs, and ω_{r} the resonance frequency.

In our description of $\hat{\sigma}_{\mathrm{tot}}(\omega)$, we obtain the initial substrate charge density N_{s} from the magnitude of the instantaneous (near 0 ps) conductivity. The bulk scattering time τ_{s} corresponding to the inferred value of N_{s} is determined independently from calibration measurements exciting the substrate at varying charge densities. In this manner the contribution of $\hat{\sigma}_{\mathrm{bulk}}(\omega)$ can be determined independently, and the parameters determining $\hat{\sigma}_{\mathrm{nw}}(\omega)$ can be readily determined from the data.

Figure 3a shows an exemplary fit to data obtained exciting the NWs using p-polarized light, for a pump−probe delay time of 10 ps, for which τ_{s} = 170 fs. The Drude contribution is
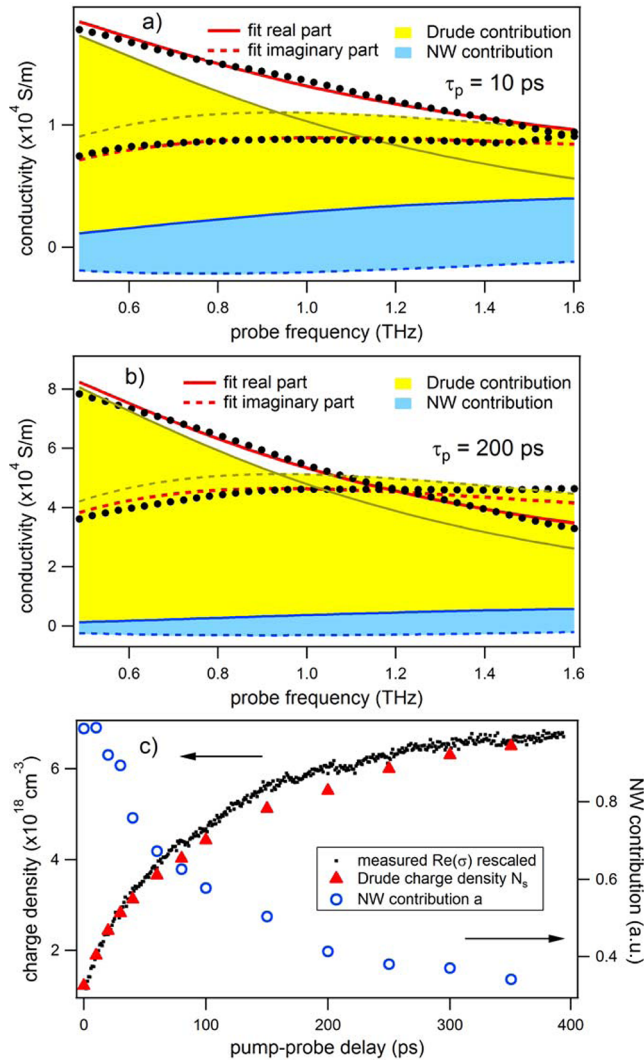

Figure 3. Complex THz photoconductivity (black dots) for NW excitation at pump−probe delay of (a) 10 ps and (b) 200 ps. Red lines show the fit to the two-component model and the yellow and blue shaded areas the Drude and NW contribution, respectively. (c) The corresponding real-conductivity dynamics (black dots) and the extracted model parameters: filled triangle = substrate charge density N; open circles = NW contribution a.

clearly dominating the signal, with only the low-frequency tail of the NW contribution appearing in the THz probe window. Figure 3b, which shows the same measurement for τ_{p} = 200 ps, demonstrates that the contribution of the Drude component originating from the substrate charge density N_{s} has increased by a factor 3, while the nanowire contribution has decreased by a similar factor. Figure 3c summarizes the extracted Drude charge densities N_{s} and the magnitude a of the NW response at various pump−probe delays for the THz dynamics depicted by the black dots, rescaled to match N_{s} for clarity. As can be seen, the increase in the real conductivity originates from an increase in the charge density in the substrate. At the same time, a is decreasing, indicating depletion of carriers in the NWs. It is apparent that the observed THz conductivity increase observed in Figure 2 when exciting the NWs are due to diffusion of charge carriers from the NWs into the bulk, where the carriers exhibit a larger response in our frequency window. Figure 3 further shows that the signal in the dynamics as measured in Figure 2, which is the real conductivity at 0.6 THz, is dominated by the Drude response of the substrate carriers. Hence, we can thus use this type of measurement as a means to infer the time-dependent charge density in the substrate, a quantity which is governed by diffusion and trapping.

In order to quantify the diffusion and trapping dynamics, we constructed a time-dependent diffusion model in COMSOL which considers the sample geometry and the charge density profile that is generated by the excitation beam as the starting condition. In the model, the excitation photon flux Φ_0 can be adjusted and the fraction of excitation light that is directly absorbed in the NWs α_{nw}. For α_{nw} = 1 all light is absorbed in the NW layer; for α_{nw} = 0 the absorption is limited to the bulk substrate. In the experiments this parameter can be modified by exciting the front or back of the sample and, for front excitation, by rotating the pump polarization. The initial density of photoexcited carriers in the NWs (N_{nw}) and the substrate (N_{sub}) are derived from Φ_0 and α_{nw}. The reflection of the pump beam at the NW−substrate interface is also taken into account. The refractive index of bulk silicon at 266 nm is 2.45, and effective-medium calculations show that, due to the SiO_2 filling between the wires, the refractive index of the NW layer is 1.53 for p-polarization and 1.71 for s-polarization. Hence, we use 1% reflection for p-polarized light and 8% for s-polarized light. The small reflective losses explain the large long-time signal in Figure 2. The NW trap density N_{t} and the diffusion constant D enter as simulation parameters. The inclusion of N_{t} is necessary given the observation that for low N_{nw} less carriers are injected from the NWs into the substrate, until below a certain density no more injection occurs (Figure 2). Trapping centers are identified as midgap states at the NW surface.

The inset of Figure 4 shows the geometry used for the simulation. Two NWs with appropriate dimensions are attached to the bulk substrate. Both NWs have a trap reservoir attached to them in which a controlled amount of carriers can diffuse into, thereby getting trapped. At τ_{p} = 0 the initial charge density profile is created, as shown in the main window of Figure 4. It shows the charge density distribution along the x-axis in NWs and bulk (interface at x = 500 nm) for a number of pump−probe delays. The numbers next to the traces indicate the pump−probe delay in picoseconds. The total charge density is split and assigned to the NWs and the substrate by considering the reflection at the NW−substrate interface and α_{nw}. The large spike in the charge density at the NW−bulk interface at τ_{p} = 0 is due to the short excitation light penetration
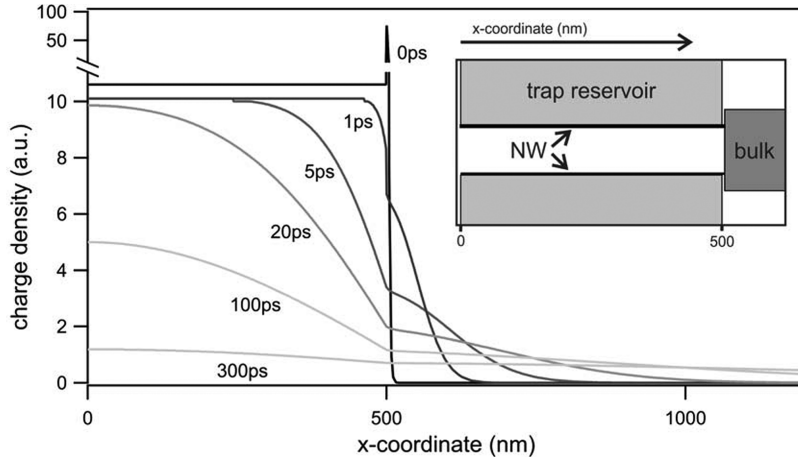
Figure 4. Simulated time evolution of the charge density for various pump−probe delays in picoseconds, indicated by the numbers next to the traces. NWs are located in the range 0 < x < 500 nm and bulk Si for x > 500 nm. The inset sketches the geometry used for the simulations. Two NWs are attached to the substrate and one trap reservoir to each NW in which charge carriers are trapped.

depth of 5 nm and the resulting strong confinement of the charge density in the x-direction. Recent ultrafast transient absorption measurements on silicon NWs[17] have shown that trapping occurs appreciably faster (~10 ps) than diffusion into the bulk (~100 ps). Accordingly, we allow a charge density corresponding to N_t to be withdrawn from the NWs into the trap reservoir within the first picosecond. This results in a homogeneous reduction of N_{nw} along the NW. In the depicted case, 3.8% of N_{nw} was subtracted. The inclusion of a longer trapping time in our model merely leads to a slight speedup of the diffusion process on the time scale of the trapping process but does not affect the value of N_t. As time progresses, charges diffuse into the substrate until equilibrium between the two material components is reached. The time-dependent, spatially integrated charge density in the bulk is proportional to the measured THz signal.

To quantify the charge carrier transfer efficiency from the NWs into the bulk, we define the quantity $A = 1 - \mathrm{Re}[\sigma(\tau=0\ \mathrm{ps})]/\mathrm{Re}[\sigma(\tau=400\ \mathrm{ps})]$. It quantifies the fraction of charge carriers in the bulk at long pump−probe delay times that originate from the NWs. $A = 0$ represents the situation where all carriers were directly excited in the bulk, and none originate from the NWs; i.e., no photoconductivity increase is observed after $\tau_p = 0$. $A = 1$ corresponds to zero initial photoconductivity; i.e., no carriers are directly excited in the bulk, and all carriers in the bulk at late pump−probe delays originate from the NWs. For initial NW carrier densities N_{nw} much larger than the trap density N_t most traps are immediately saturated. The diffusion dynamics in this scenario are unaffected by the trapping process, and A only depends on the fraction of excitation light directly absorbed in the NWs, α_{nw}. Hence, determining A from the dynamics at high fluence provides a way to estimate α_{nw}. For p-polarized excitation, $\alpha_{nw} \approx 0.87$ and $A \approx 0.8$ for high excitation fluences. The s-polarized excitation gives A around 0.55 and $\alpha_{nw} \approx 0.6$. When N_{nw} is lowered by decreasing Φ_0 and becomes comparable to N_t, A decreases and eventually reaches values of zero when most carriers become trapped in the wires and hence no injection from the wires into the bulk occurs. Sweeping Φ_0 through this regime in the experiment thus provides a means to determine N_t.

Figure 5 shows data and the matching simulations for exactly this procedure. Φ_0 was changed by a factor of about 30 in the experiments. The upper (lower) panel displays results for s (p)-
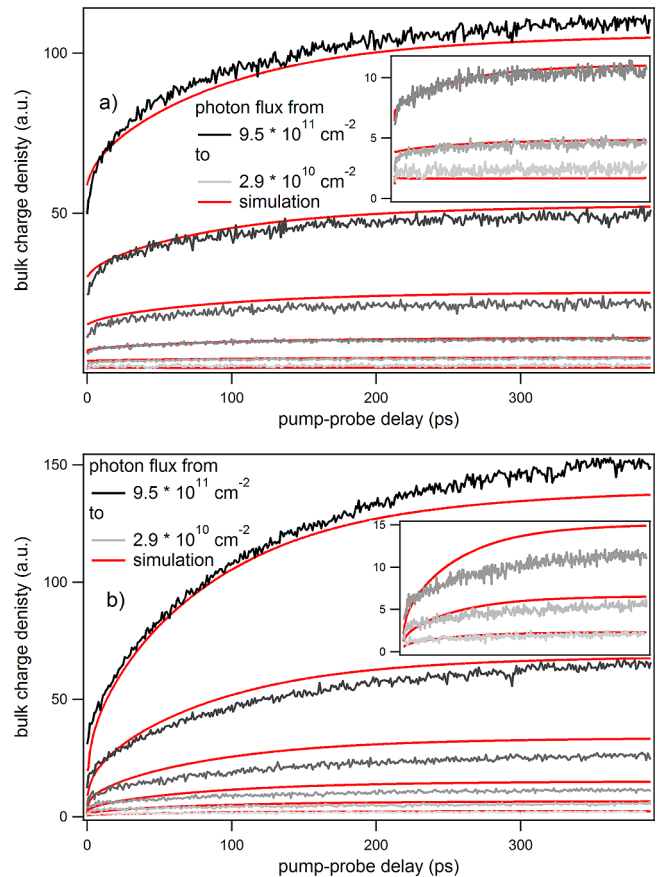

Figure 5. Time-resolved substrate charge density for various photon fluxes Φ_0: (a) s-polarized excitation and (b) p-polarized excitation. Red lines depict the results of the diffusion model. The inset shows a magnified view of the three lowest Φ_0.

polarized excitation where α_{nw} = 0.6 (0.87). Note that no adjustments were made for Φ_0 in the simulations with respect to the experimental pump fluence. The deviations for some traces concerning the magnitude of the real conductivity are therefore due to experimental uncertainties in the determined fluence.

For the highest excitation density, $N_{nw} \gg N_t$, trapping is negligible. For the s-polarized excitation case only 3.8% of the

generated carriers in the NW are trapped. The injection time is largely constant and depends in the model only on the diffusion constant which was found to be 12 ± 2 cm^2/s. This is about a factor 3 lower than the bulk diffusion constant, which we calculate to be around 30 cm^2/s for electrons by taking the measured bulk Drude scattering time of 170 fs and using the Einstein diffusion relation $D = kT\tau_s/m^*$, where k is the Boltzmann constant and T room temperature. The reduction of diffusivity is expected when going from bulk to an essentially one-dimensional diffusion mechanism in the nanowire: the electron mean free path in the bulk is around 40 nm and larger than the wire diameter. Carrier scattering with the boundary becomes thus more dominant in the NWs, leading to the observed reduction in diffusivity. The inset of Figure 5a shows a magnified view of the three lowest photon fluxes. One can see that A is decreasing for decreasing Φ_0, reaching zero for 2.9×10^{10} cm^{-2}, corresponding to 100% trapped carriers. We note that for this lowest photon flux on average only one to two carriers are excited per NW. We obtain a trap density of $N_t = (4.5 \pm 1.5) \times 10^9$ cm^{-2}, which in turn indeed corresponds to the presence of only one to two active traps per NW on average.

We also measured a sample (sample 2) with the same NW diameters, however treated with a forming-gas anneal step, which is supposed to improve the surface passivation. Indeed, a 2-fold decrease in trap density is found as compared to sample 1, down to $N_t = (2.0 \pm 1.0) \times 10^9$ cm^{-2}.

The values of our trap densities are comparable to previously published results on similarly passivated silicon NWs,[18] which might however be coincidental. The authors inferred the trap density from measurements of the photoluminescence decay rate of photoexcited electron−hole liquid (EHL) droplets, which was on the order of 100 ns, as a function of NW diameter, and used literature room-temperature capture cross sections (CCS) to eventually obtain the trap density. The experimental conditions the authors used were however different to ours: first, the sample was held at a temperature of 10 K, which can already alter the CCS and thus the inferred trap density. Also, even though no exact statements were given on the pump fluence and on the photogenerated charge density, they were presumably orders of magnitude larger than our values, for such magnitudes are required in order to reach the EHL phase.[19] Furthermore, a pulsed laser with nanosecond pulse duration was used. Given previously reported trapping times of around 10 ps,[17] these excitation conditions, i.e., high pump fluences over nanosecond time scales, will give rise to trap filling already during the excitation process. That would mean that the measured recombination dynamics will be convoluted with the time scale of the occupied traps returning to their equilibrium state, thus increasing the EHL recombination time. In contrast, our measurements probe the trapping process in a more direct fashion. The femtosecond excitation process is quasi-instantaneous with respect to trap-filling times, and nontrapped carriers are directly "counted" through their THz photoconductivity after injection into the bulk.

Interestingly, the inferred trap density is much lower than the density of midgap states, which originate from unpassivated silicon dangling bonds and which are the most probable source for trapping. Some of us have previously performed ESR measurements on similarly passivated NWs with a mean diameter of 10 nm,[7] which yielded a defect density of about 1×10^{12} cm^{-2}, i.e., about 2 orders of magnitude larger than the trap density inferred here. The defect density of the 25 nm NWs

investigated here is presumably lower but likely to be of the same order of magnitude: smaller diameter NWs possess a higher curvature and thus more strained Si−O bonds, leading possibly to more dangling bonds. The large discrepancy between trap density and surface defect density indicates that not all midgap states act as carrier traps. Indeed, a previous study using pulsed photoluminescence has already shown that silicon dangling bonds of unstrained reconstructed bulk silicon surfaces are not recombination-active.[20] A similar situation might occur here for some defects, although the large strain in the nanowires presumably creates unsaturated silicon bonds beneath the surface whose dangling bonds in turn form active recombination centers.[20]

On the other hand, our measurements are only sensitive to trapping occurring on picosecond time scales, which is a reasonable time frame with respect to commonly accepted defect CCSs and recent ultrafast measurements on carrier-defect recombination in bulk and nanostructured semi-conductors.[21−23] It is however conceivable that the apparent low trap density originates from a dramatic decrease in the CCS. Interface effects such as the Coulomb blockade screening mechanism, which is known to occur at the Si−SiO$_2$ interface and which has been well-studied in short-channel bulk silicon[24] and silicon NW field-effect transistors,[25] can lead to a dramatic reduction of the CCS, particularly at the extremely low charge densities present here.[26] On that account, the specification of a trap density is somewhat meaningless without knowledge of the CCS and vice versa. We thus cannot fully conclude on whether all midgap states are electrically active, albeit with a reduced CCS, or whether only some of them are active possessing large CCSs.

Irrespective of the actual trapping mechanism, the possible existence of traps that are not accessible with our measurement approach or other effects that could inhibit diffusion, the minimum charge density as measured here at which diffusion allows carriers to escape the nanowire constitutes a key figure of merit since it will determine the potential of using the NWs as active material in devices (e.g., solar cells) that rely on diffusion. In order to extract a photocurrent from the NWs, it must be possible to collect the majority of generated carriers. Our measurements however suggest that when the fluence is reduced, the majority of carriers generated in the NWs are trapped within the first few picoseconds. For the lowest pump fluence in our measurements (30 nJ/cm^2) all carriers that were generated in the wires, which is on average only one to two carriers per NW, are trapped, and no significant amount of carriers is injected into the bulk. It is therefore evident that many carriers need to be present in a single NW simultaneously for traps to be passivated; otherwise, no photocurrent will be collected from a solar cell with thin silicon NWs as the active material. If one assumes a trapping time of 10 ps, the fluence of 30 nJ/cm^2 translates to a minimum power density of 3 kW/cm^2 that is required to fill traps in order to inject the remaining carriers into the bulk. This is orders of magnitude larger than the 100 mW/cm^2 power from the AM1.5 spectrum.

This conclusion might seem in variance with recently published results on silicon NW solar cells for which good efficiencies were demonstrated.[5,27] These devices however relied on appreciably thicker NWs with diameters of about 1 μm, where the influence of surface defects is greatly reduced,[5] or NWs of about 200 nm diameter with a coaxial p-i-n structure which reduces the diffusion length of minority carriers and screens them from surface defects.[27] Devices that would rely on

much thinner silicon NWs such as the ones investigated here, for instance in order to exploit quantum confinement effects, will require greatly reducing the impact of trapping. It is likely that NWs made of different semiconductors but comparable diameters will face similar challenges.

Conclusion. We have measured the diffusion dynamics of photogenerated charge carriers in an ordered silicon NW array on bulk silicon. We observe that charge carriers, which are excited in the NWs by a femtosecond UV pulse, diffuse into the bulk on tens to hundreds picosecond time scales. For sufficiently low excitation fluences this diffusion process stalls because the majority of charge carriers become trapped at NW surface defects. Using a model that simulates the diffusion process, we extracted parameters such as the diffusion constant and the NW trap density. The trap density was found to be 2 orders of magnitude smaller than the density of surface defects that are commonly identified as carrier traps. This suggests that either only a small part of surface defects can actually scavenge charge carriers or that screening mechanisms reduce the capture cross section. Irrespective of the mechanism, the charge density at which diffusion stalls is orders of magnitude larger than what would be generated by sunlight. Hence, in order to collect photoexcited charge carriers using these thin silicon NWs as active material in a solar cell, surface defect passivation must be dramatically improved.

■ AUTHOR INFORMATION

Corresponding Author
*E-mail: bonn@mpip-mainz.mpg.de.

Notes
The authors declare no competing financial interest.

■ ACKNOWLEDGMENTS

■ REFERENCES

(1) Garnett, E. C.; Brongersma, M. L.; Cui, Y.; McGehee, M. D. *Nanowire Sol. Cells* **2011**, *41*, xxxx.

(2) Garnett, E.; Yang, P. *Nano Lett.* **2010**, *10*, 1082.

(3) Srivastava, S. K.; Kumar, D.; Singh, P. K.; Kar, M.; Kumar, V.; Husain, M. *Sol. Energy Mater. Sol. Cells* **2010**, *94*, 1506.

(4) Kayes, B. M.; Atwater, H. A.; Lewis, N. S. *J. Appl. Phys.* **2005**, 97.

(5) Kelzenberg, M. D.; Boettcher, S. W.; Petykiewicz, J. A.; Turner-Evans, D. B.; Putnam, M. C.; Warren, E. L.; Spurgeon, J. M.; Briggs, R. M.; Lewis, N. S.; Atwater, H. A. *Nat. Mater.* **2010**, *9*, 239.

(6) Yoon, H. P.; Yuwen, Y. A.; Kendrick, C. E.; Barber, G. D.; Podraza, N. J.; Redwing, J. M.; Mallouk, T. E.; Wronski, C. R.; Mayer, T. S. *Appl. Phys. Lett.* **2010**, *96*, xxxx.

(7) Jivanescu, M.; Stesmans, A.; Kurstjens, R.; Dross, F. *Appl. Phys. Lett.* **2012**, *100*, 082110.

(8) Ulbricht, R.; Hendry, E.; Shan, J.; Heinz, T. F.; Bonn, M. *Rev. Mod. Phys.* **2011**, *83*, 543.

(9) Hendry, E.; Koeberg, M.; Schins, J. M.; Nienhuys, H. K.; Sundstrom, V.; Siebbeles, L. D. A.; Bonn, M. *Phys. Rev. B* **2005**, *71*, 125201.

(10) Drude, P. *Ann. Phys.* **1900**, *308*, 369.

(11) Hendry, E.; Koeberg, M.; Pijpers, J.; Bonn, M. *Phys. Rev. B* **2007**, *75*, 233202.

(12) Nienhuys, H. K.; Sundstrom, V. *Appl. Phys. Lett.* **2005**, *87*, 012101.

(13) Parkinson, P.; Lloyd-Hughes, J.; Gao, Q.; Tan, H. H.; Jagadish, C.; Johnston, M. B.; Herz, L. M. *Nano Lett.* **2007**, *7*, 2162.

(14) Strait, J. H.; George, P. A.; Levendorf, M.; Blood-Forsythe, M.; Rana, F.; Park, J. *Nano Lett.* **2009**, *9*, 2967.

(15) Hendry, E.; Koeberg, M.; O'Regan, B.; Bonn, M. *Nano Lett.* **2006**, *6*, 755.

(16) Smith, N. V. *Phys. Rev. B* **2001**, *6415*, 155106.

(17) Kar, A.; Upadhya, P. C.; Dayeh, S. A.; Picraux, S. T.; Taylor, A. J.; Prasankumar, R. P. *IEEE J. Sel. Top. Quantum Electron.* **2011**, *17*, 889.

(18) Demichel, O.; Calvo, V.; Besson, A.; Noe, P.; Salem, B.; Pauc, N.; Oehler, F.; Gentile, P.; Magnea, N. *Nano Lett.* **2010**, *10*, 2323.

(19) Suzuki, T.; Shimano, R. *Phys. Rev. Lett.* **2009**, *103*, 057401.

(20) Dittrich, T.; Bitzer, T.; Rada, T.; Timoshenko, V. Y.; Rappich, J. *Solid-State Electron.* **2002**, *46*, 1863.

(21) Seo, M. A.; Dayeh, S. A.; Upadhya, P. C.; Martinez, J. A.; Swartzentruber, B. S.; Picraux, S. T.; Taylor, A. J.; Prasankumar, R. P. *Appl. Phys. Lett.* **2012**, *100*, xxxx.

(22) Ulbricht, R.; van der Post, S. T.; Goss, J. P.; Briddon, P. R.; Jones, R.; Khan, R. U. A.; Bonn, M. *Phys. Rev. B* **2011**, *84*, xxxx.

(23) Jepsen, P. U.; Schairer, W.; Libon, I. H.; Lemmer, U.; Hecker, N. E.; Birkholz, M.; Lips, K.; Schall, M. *Appl. Phys. Lett.* **2001**, *79*, 1291.

(24) Mueller, H. H.; Schulz, M. *J. Mater. Sci.: Mater. Electron.* **1995**, *6*, 65.

(25) Zhuge, J.; Zhang, L.; Wang, R.; Huang, R.; Kim, D.-W.; Park, D.; Wang, Y. *Appl. Phys. Lett.* **2009**, *94*, 083503.

(26) Mueller, H. H.; Worle, D.; Schulz, M. *J. Appl. Phys.* **1994**, *75*, 2970.

(27) Tian, B.; Zheng, X.; Kempa, T. J.; Fang, Y.; Yu, N.; Yu, G.; Huang, J.; Lieber, C. M. *Nature* **2007**, *449*, 885.